CHEMISTRY OF MATERIALS

Article

pubs.acs.org/cm

Dimensionally Controlled Lithiation of Chromium Oxide

Tim T. Fister,[*,†] Xianyi Hu,[‡,∥] Jennifer Esbenshade,[§] Xiao Chen,[#] Jinsong Wu,[‡] Vinayak Dravid,[‡] Michael Bedzyk,[‡,#] Brandon Long,[†,§] Andrew A. Gewirth,[§] Bing Shi,[⊥] Christian M. Schlepütz,[⊥] and Paul Fenter[†]

[†]Chemical Sciences and Engineering Division and [⊥]X-ray Science Division, Argonne National Laboratory, Argonne, Illinois 60439, United States

[‡]Materials Science & Engineering Department and [#]Applied Physics Program, Northwestern University, Evanston, Illinois 60208, United States

[§]Chemistry Department, University of Illinois, Urbana−Champaign, Illinois 61801, United States

Supporting Information

ABSTRACT: Oxide conversion reactions are an alternative approach for high capacity lithium ion batteries but are known to suffer from structural irreversibility associated with the phase separation and reconstitution of reduced metal species and Li_2O. In particular, the morphology of the reduced metal species is thought to play a critical role in the electrochemical properties of a conversion material. Here we use a model electrode with alternating layers of chromium and chromium oxide to better understand and control these phase changes in real-time and at molecular length scales. Despite lacking crystallinity at the atomic scale, this superstructure is observed (with X-ray reflectivity, XR) to lithiate and delithiate in a purely one-dimensional manner, preserving the layered structure. The XR data show that the metal layers act as nucleation sites for the reduction of chromium in the conversion reaction. Irreversibility during delithiation is due to the formation of a ternary phase, $LiCrO_2$, which can be further delithiated at higher potentials. The results reveal that the combination of confining lithiation to nanoscale sheets of Li_2O and the availability of reaction sites in the metal layers in the layered structure is a strategy for improving the reversibility and mass transport properties that can be used in a wide range of conversion materials.

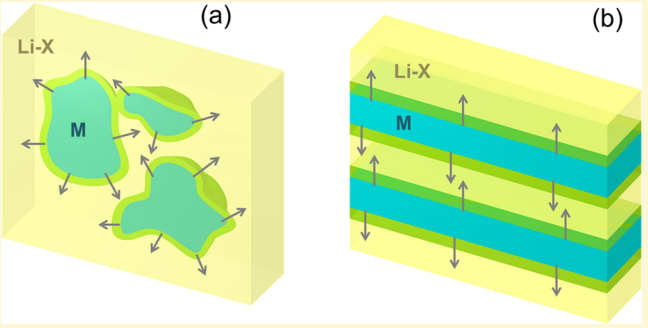

INTRODUCTION

Intercalation materials have long been the foundation for commercial lithium ion batteries (LIBs) but are intrinsically limited in charge capacity by the number of Li sites necessary to preserve the electrodes' crystal structure during cycling.[1] Conversion reactions of MX compounds (M = metal and X = O^{2-}, S^{2-}, F^-, P^{3-}, etc.), such as the well-known phase separation of a metal oxide into Li_2O and reduced metal species (e.g., $MO_x + 2xLi^+ \leftrightarrow M + xLi_2O$),[2] provide an alternative storage mechanism that is not limited by the electrode crystal structure. As a result, conversion reactions are capable of multiple electron transfers with higher specific capacity than intercalation materials.[3,4] However, these reactions typically have multiple challenges, including reduced discharge plateaus well below Nernstian behavior, significant overpotentials, sluggish kinetics, and large volume changes that can reduce particle cohesion, much like intermetallic reactions found in Si and Sn electrodes.[5,6] Each of these factors has been attributed to competition between interfacial and bulk thermodynamics[7] and is highly dependent on electrode morphology.[8]

During lithiation, conversion leads to phase-separated lithium-rich and reduced metal species, as depicted in Figure 1a. Ideally, this phase separation occurs at the nanoscale, providing a high concentration of interfaces and short interparticle diffusion lengths that would enable reversibility.[9] As illustrated in Figure 1a, the metal species typically nucleate

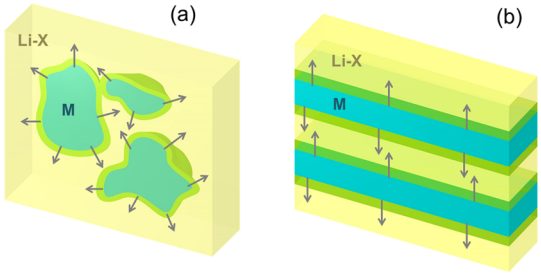

Figure 1. Illustration of phase separation for (a) bulk and (b) layered conversion reactions. The nucleated metal species (M), lithiated phase (Li-X), and their interfaces are indicated by the blue, yellow, and green components respectively with arrows indicating the growth direction of the metal species.

Received: May 14, 2015
Revised: November 23, 2015
Published: November 23, 2015

DOI: 10.1021/acs.chemmater.5b01809
Chem. Mater. 2016, 28, 47−54

as 2−5 nm nanoparticles embedded in an amorphous Li-rich matrix.[2] This nanophase morphology plays a significant role in these reactions: both at the onset, where partial [re]oxidation of the metal species impedes both charge and mass transport, leading to substantial irreversibility and overpotentials during the first cycle; and over time, where particle ripening can gradually slow mass transfer at the Li_nX-M interface.[10] The interface itself is also thought to play a significant role for electronic transport across and electrocatalysis at the metal/lithia interface and for ionic transport (of both Li^+ and O^{2-}). Additional charge storage mechanisms have been attributed to this region as well. However, a fundamental understanding of electrochemical processes at these interfaces has been stymied by the difficulties accessing the extreme environment of a LIB and the inherent, three-dimensional complexity of a reacting conversion material.

To better understand the role of interfaces in conversion reactions, we study a model electrode consisting of well-defined, vertically aligned layers of Cr and CrO_x, like those depicted in Figure 1b. This type of heterostructure is ideal for X-ray reflectivity (XR) which is directly sensitive to interfacial structure and reactivity and can be measured *in situ* with Ångstrom vertical resolution. Remarkably, we show that the initial nanoscale layering in the electrode provides a template for guiding the subsequent conversion reaction, in that the metal layers act as pre-existing nucleation sites for the reduction of the metal oxide reducing the barrier for reaction. This effectively confines the Li_2O and Cr products, providing a well-defined architecture for delithiation. The stability of the architecture is suggested by the observation that the internal electrode layering becomes even more pronounced during subsequent cycling and is amenable to aggressive charge/discharge conditions. These results point to a possible new strategy for controlling the morphology of conversion materials during electrochemical cycling.

EXPERIMENT

The thin film sample was grown by DC magnetron sputtering at room temperature as a silicon/chromium bilayer on R-plane sapphire. As described more fully in the Supporting Information, the 10 × 3 mm^2 sample was immersed in an electrolyte of 1.0 M $LiPF_6$ in 1:1 ethylene carbonate/dimethyl carbonate during the *in situ* measurements. Chronoamperometric measurements were performed using the sample as the working electrode and separate lithium counter and reference electrodes. We also characterized the as-grown samples using X-ray reflectivity (XR), transmission electron microscopy (TEM), and depth-resolved X-ray photoelectron spectroscopy (XPS). XR was measured at the Advanced Photon Source, sector 33BM at 20 keV (λ = 0.6198 Å) using a four-circle diffractometer and area detector (Pilatus 100k).[11] The beam was focused and collimated to 1.5 × 0.2 mm^2 at the sample and illuminates a 1.5 × 3 mm^2 area on the electrode surface. As shown by rocking curves collected during the lithiation/delithiation process (Figure S7 in the Supporting Information), the scattered X-rays showed no signs of broadening or diffuse scattering during the entire measurement, indicating that changes to the vertical structure of the sample were laterally uniform within the footprint of the beam.

As shown in Figures 2a and 2b, the Si/Cr bilayer was found to have significant structural density modulations within the buried metal layer. As seen in Figure 2b, fits to the reflectivity indicated that the buried chromium film actually consisted of alternating 10.2 Å-thick layers with densities ranging from 1.5 to 1.8 $e^-/Å^3$ (±0.05 $e^-/Å^3$), buried beneath a silicon capping layer. These range from the density of bulk Cr_2O_3 up to densities approaching chromium metal. This type of layering gives rise to a weak multilayer diffraction peak in the XR data (Figure 2a). This broad feature is centered at q = 0.28 $Å^{-1}$ with a full-width Δq = 0.046 $Å^{-1}$ and is indicative of a repeated multilayer structure with "d-spacing" of $2\pi/(q^2 - q_c^2)^{1/2} \approx$ 20.4 Å and six repeated bilayers, in close agreement with the extracted density profile.

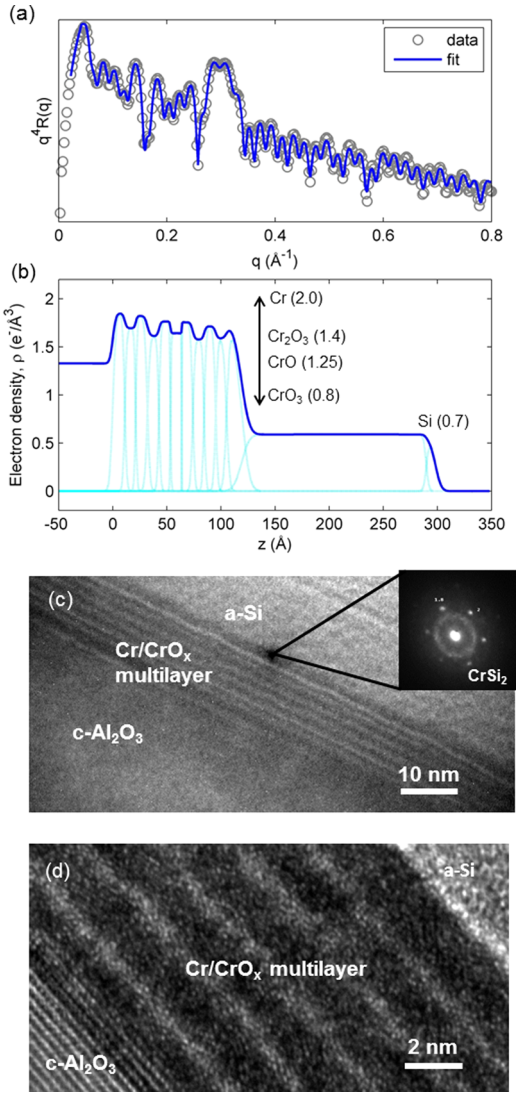

Figure 2. Characterization of the initial film by (a) X-ray reflectivity (XR) and (c-d) transmission electron microscopy (TEM) confirms the underlying layered structure. The fit to the reflectivity shown in (a) corresponds to the layered slab model shown in (b). The electron density in the multilayer region is between the bulk Cr and Cr_2O_3 values. TEM (c and inset, d) confirm this overall structure and the lack of crystallinity in each layer. The XR data were fit to a layered slab model using a genetic algorithm approach and then refined using traditional nonlinear regression.[12]The electrode structure shown in (b), consisting of alternating 10.2 Å-thick layers with densities ranging from 1.5−1.8 e-/$Å^3$ (±0.1 e-/$Å^3$), was determined by balancing the overall quality of fit with the propagated errors in the density profile, as previously discussed.[13]All parameters (thickness, density, and interfacial roughness) were allowed to vary except for the known densities of the sapphire substrate and electrolyte.

TEM results (Figures 2c and 2d) confirmed the layering in the underlying chromium layer. The sample was found to be amorphous apart from weak crystalline $CrSi_2$ electron diffraction found at the Si/Cr interface. From the XR and TEM measurements, which only are sensitive to the total electron density, it was unclear whether the initial modulated density was due to silicon/chromium intermixing or the presence of an oxide or other impurity. The sample was also analyzed using depth resolved XPS (as shown in the Supporting Information),

DOI: 10.1021/acs.chemmater.5b01809
Chem. Mater. 2016, 28, 47−54

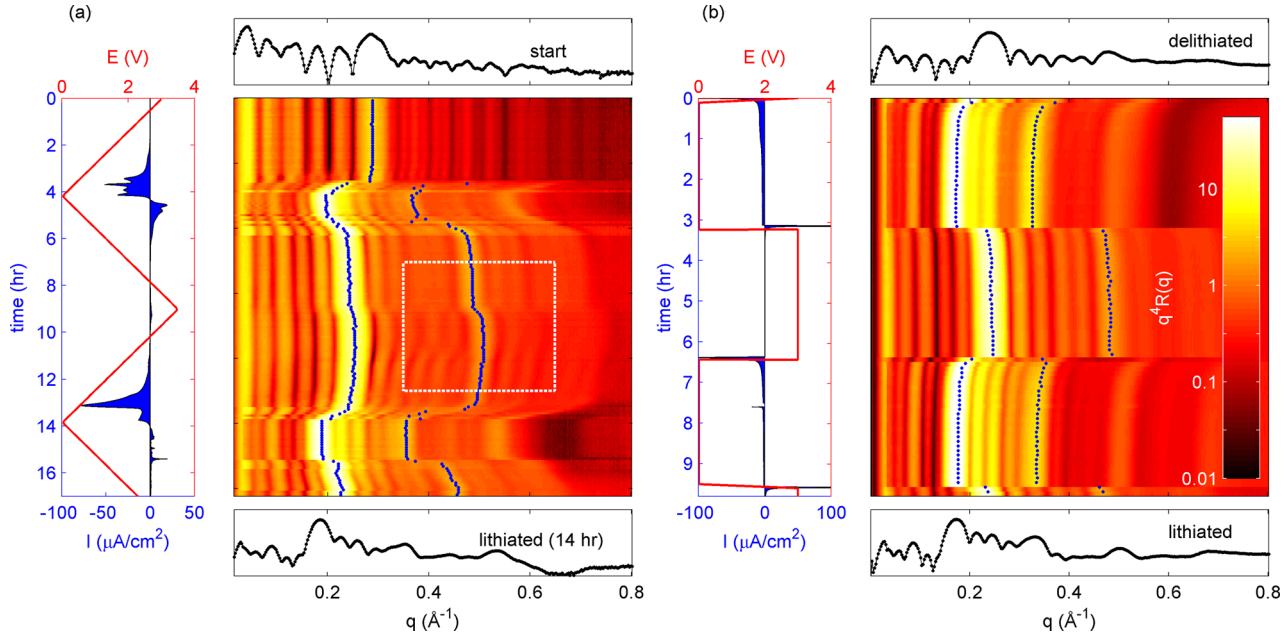

Figure 3. Real-time, normalized XR plotted during (a) cyclic voltammetry and (b) potential step measurements. In each case the electrochemical data are shown on the left, and the reflectivity intensity is indicated by a logarithmic color scale (shown on the right). Note that the applied potential E and the measured current I are overlaid and have different axis ranges, as noted. The color scale on the reflectivity scales logarithmically from $q4R(q) = 0.01-50$. The first and second order Bragg peaks are indicated by the blue points on each plot to highlight the coherent expansion and contraction of the CrOx multilayer during lithiation and delithiation. A subset of the reflectivity marked by a box in (a) is shown in Figure 4.

which confirmed that only Si, Cr, and O are present in the film and that both the oxygen and chromium core-loss spectra are consistent with a mixed Cr/CrO_x phase in the layered region. Consequently, this thin-film structure provides an ideal architecture for understanding conversion reactions without the complications of the crystallinity.

RESULTS

Having delineated the structure and components present in the film using *ex situ* methods, we proceeded to observe the thin-film structure with *in situ* XR as a function of electrochemical potential (E, reported as V vs Li/Li^+) during lithiation/delithiation reactions using a custom X-ray-compatible electrochemical cell (described in the Supporting Information). We compared structural changes during a gradual potential sweep (ΔE = 0.2 mV/s) and in response to a large potential step between 3 and 0.02 V. Changes in the normalized reflectivity in both cases are shown in the color plot versus time in Figure 3. The dominant feature throughout the reaction is the multilayer Bragg peak, which shifts to lower and higher q as the multilayer expands and contracts during lithiation and delithiation, respectively. In Figure 3, the position of the peak's maximum (and its second order diffraction peak) are tracked with blue dots as a guide. The persistence and intensification of the diffraction peak at all conditions indicate that the layering is preserved throughout the lithiation and delithiation reactions, despite vertical expansion and contraction by up to 50%.

Much like "bulk" conversion reactions, the structural changes in the multilayer are most pronounced during the first lithiation cycle and are highly reversible thereafter. This initial conditioning can be seen during the cyclic voltammogram (CV) in Figure 2a, where there is a discontinuity in the reflectivity at 0.3 V. This is partially due to the dampening of the highest frequency oscillations corresponding to the overall thickness of the electrode from the interference of X-rays scattering from the substrate and the top silicon surface. As the silicon expands and roughens, these oscillations are diminished. Immediately following this transition at 0.3 V, the multilayer (ML) diffraction peak shifts to lower q indicating the coherent expansion of the multilayer by ~50%. Likewise, oxidative current (primarily from the delithation of the silicon capping layer at 0.1−0.5 V) precedes the positive shift of the ML Bragg peak as the structure contracts. The increase in the ML diffraction peak intensity after the first discharge is caused by stronger contrast between the lower-density lithiated layers and the higher-density metallic layers, but the persistence of this first order Bragg peak and the emergence of the higher order diffraction peaks during cycling indicates unequivocally that the ML structure remains intact throughout the conversion reaction.

Beyond the wholescale changes seen at low potential, a smaller, reversible change in the multilayer d-spacing can also be seen near the upper voltage limit (3.5 V). A portion of this region is shown in Figure 4. Such a high voltage reaction could possibly involve oxygen or the decomposition of residual Li_2O. However, closer examination of the CV reveals weak, reversible redox features at 3.3 and 1.8 V (Figure 4b) that correspond well to finer shifts in the multilayer Bragg peak corresponding to a 5% change in bilayer d-spacing. As discussed below, these changes are consistent with a new Li_xCrO_2 phase that forms after the initial discharge. The lower density of this phase (compared to Cr_2O_3) is largely responsible for the increased Bragg peak intensity and expansion of the multilayer after one full cycle.

The XR data clearly indicates the structural stability of the multilayer structure during the conversion reaction, but the alignment of the chromium layers could inhibit lithium transport. The role of lithium transport in such a layered structure was measured with real-time observations of the structural and electrochemical response to potential steps between 3 and 0.02 V. The current response to the step is

DOI: 10.1021/acs.chemmater.5b01809
Chem. Mater. 2016, 28, 47−54

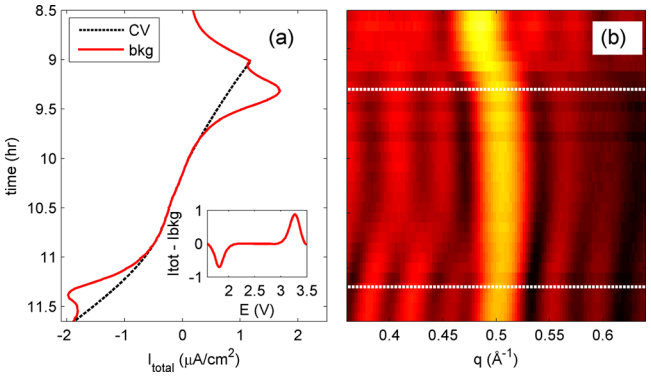

Figure 4. Redox changes at high potential from Figure 3a can be seen clearly both in the cyclic voltammetry (a) and in the reflectivity. The electrochemical data in (a) is plotted as a function of time, as in Figure 3 with a background profile given by a cubic spline extrapolated from potentials outside the redox reaction. The background subtracted CV is shown in the inset to emphasize the reversibility of the reaction. The dashed white lines in the XR data are times corresponding to the redox voltages. (b) The shift of the second order Bragg peak indicates contraction of the multilayer structure at 3.3 V by 5%, followed by a more gradual expansion near 1.8 V.

largely exponential but with fast (30−60 s) and slower (130−480 s) decay constants (Table 1), likely related to the lithiation

Table 1. Kinetics of Potential Step Measurements[a]

	Q_{tot} (mAh)	t_1 (s)	t_2 (s)	t_{XR} (s)
first lithiation	−0.00421	36.8	296	310
first delithiation	+0.00237	29.2	162	200
second lithiation	−0.00248	64.1	484	470
second delithiation	0.00200	28.6	130	NA

[a]The electrochemical response and shift in XR diffraction peak during the potential step measurements shown in Figure 3b. The response was fit to two exponentials plus an overall constant (fits to electrochemical data and reflectivity are provided in the Supporting Information). The integrated charge of the combined exponential response (Q_{tot}) and its two time scales (t_1 and t_2) are shown with the time scale of the shift in the reflectivity for comparison. For reference, the theoretical charge of 20 nm Si + 5 nm Cr_2O_3 is 0.00573 mAh/g.

of the silicon and CrO_x layers, respectively (see the Supporting Information for fits used to obtain these relaxation times). In support of this conclusion is the observation that the slower time constant coincides with the response time of the layered oxide's shifting XR Bragg peak (t_{XR}). Note that this time scale in combination with the 20 nm thickness of the silicon buffer layer gives an estimated diffusion constant of ~10^{-12} cm^2/s, in line with reported literature values for Si,[12] indicating that the rate of lithiation of the Cr_2O_3 is limited by diffusion through the entire heterostructure. This also implies that lithium transport occurs vertically through the entire thin film heterostructure, fully consistent with the lack of X-ray diffuse scattering that would otherwise indicate the presence of lateral heterogeneity (e.g., cracks for fast diffusion paths or random nucleation events). For each cycle, the positive current (corresponding to delithiation) typically has a faster time constant, most likely due to the larger applied overpotential at 3 V.

DISCUSSION

The high degree of complexity that is resolved in the XR observations of conversion reactions in this model structure raises multiple points for discussion:

Chromium Oxide Phase Identification and Nucleation. Changes in the species and size of each layer are obtained by quantitatively fitting the reflectivity data over the entire first cycle CV (Figure 3a) in a manner similar to the *ex situ* sample shown in Figure 2. The resulting electron density profiles (EDPs) at the extreme conditions (i.e., at the open circuit and following lithiation and delithiation over the first cycle and lithiation during the second cycle) are shown in Figure 5a-d. The data confirm that the multilayer structure persists throughout the reaction, as suggested by the shifting Bragg peak in Figure 3. Moreover, the thickness of both the oxide *and* metal layers increases during the first lithiation cycle, indicating that the pre-existing chromium layers act as nucleation sites for the metal reduction during the conversion reaction.

The extracted electron densities can be used to identify the species present in the reaction. Based on a comparison of the observed densities with the values of known chromium and lithium oxides (labeled in each panel of Figure 5) and the changes in each layer's thickness, we propose the following reactions:

$$Cr_2O_3 + 6Li^+ \xrightarrow{0.2\ V} 2Cr + 3Li_2O \quad \text{(i)}$$

$$2Cr + 3Li_2O \underset{0.2\ V}{\overset{\sim 1.0\ V}{\rightleftharpoons}} 1.5LiCrO_2 + 0.5Cr + 4.5Li^+ \quad \text{(ii)}$$

$$1.5LiCrO_2 + 0.5Cr \underset{1.8\ V}{\overset{3.3\ V}{\rightleftharpoons}} CrO_2 + 0.5Cr + 1.5Li^+ \quad \text{(iii)}$$

Reaction i occurs during the first discharge. As seen in Figure 5b, lithium insertion begins to lower the oxide layer's electron density, while the nominal metal layers densify and increase in thickness from the displacement reaction. Note that the phase separation of low density Li_2O and the Cr species is most pronounced near the surface of the oxide multilayer, as might be expected with vertical transport through the ML structure. The theoretical volume change of reaction i is 92%, which is in line with the measured volume changes since roughly half of the heterostructure reacts with lithium.

Reaction ii connects the profiles seen in Figure 5b and 5c. Conversion reactions are, with few exceptions,[13] irreversible during the first cycle, often stopping at the first stable oxidation state during delithiation. Along these lines, previous authors suggested that divalent CrO was the delithiated phase,[14,15] in analogy to the lithation of cobalt[16] and iron oxides,[17] i.e.

$$2Cr + 3Li_2O \leftrightarrow 4Li + 2CrO + Li_2O$$

instead of reaction ii. Based solely on the extracted electron density alone, we cannot identify which phase is present since CrO and $LiCrO_2$ have similar densities that are both in line with our results. However, such a reaction would lead to some residual Li_2O and that the metal layers would return to their original thickness or even smaller if adjacent metal layers became partially oxidized. Instead, we find that the oxide layers are nearly the same thickness and that the metal layers are thicker than at the start. This finding is summarized in Table 2 and is highlighted by the marked layers in Figure 5. Also, we see no evidence for any residual, lower density Li_2O phase in the delithiated structures. Furthermore, $LiCrO_2$ is also the most stable phase in the Li/Cr/O phase diagram, whereas CrO is

DOI: 10.1021/acs.chemmater.5b01809
Chem. Mater. 2016, 28, 47−54

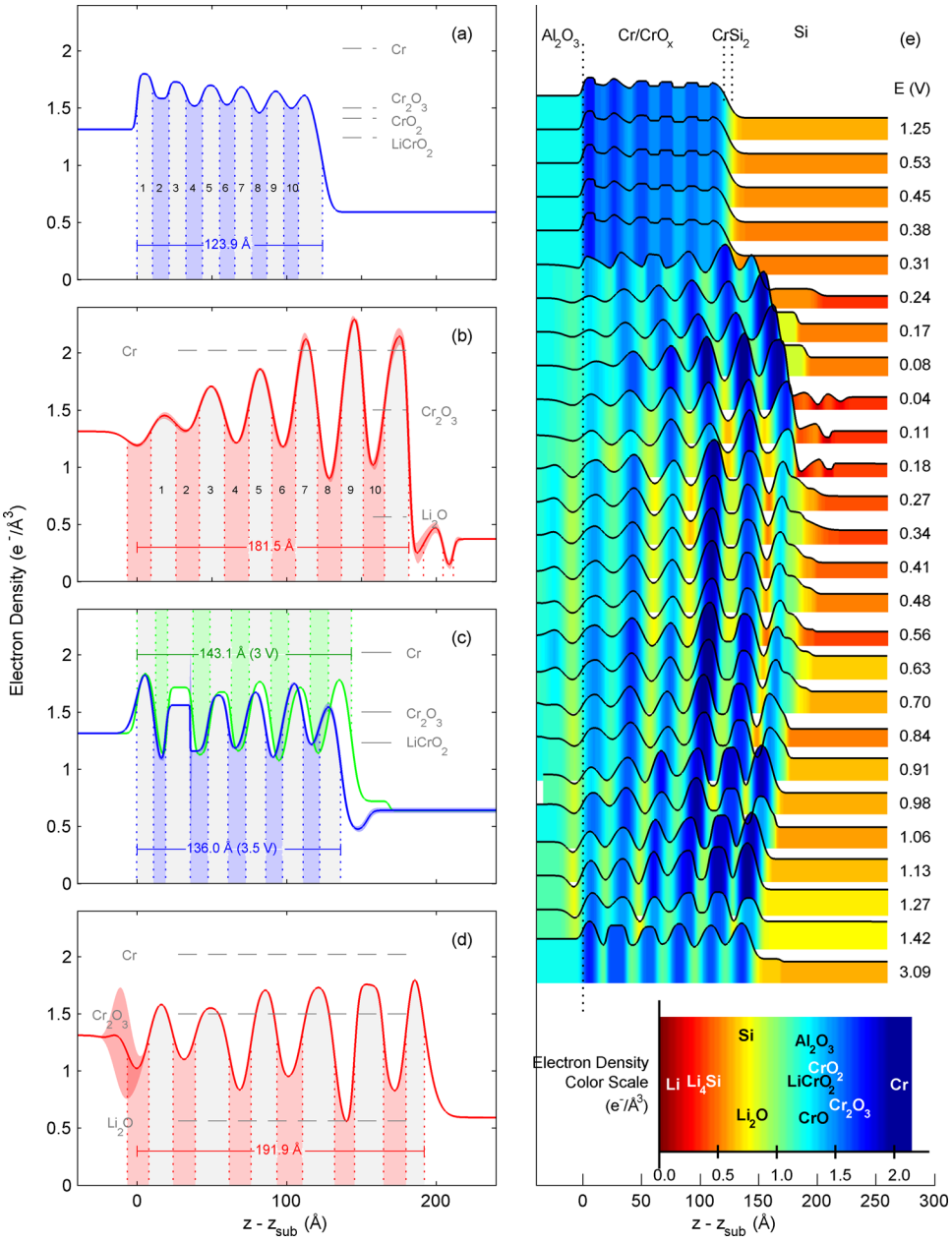

Figure 5. Extracted electron density profiles from the XR data in Figure 3a at (a) the open circuit condition, (b) at 0.035 V during the first lithiation, (c) 3 and 3.5 V during the first delithiation, and (d) 0.035 V during the second lithiation. EDPs at intermediate conditions during the first lithiation cycle are vertically staggered in (e) to highlight the evolution of the multilayer structure and the changing density of the silicon overlayer. In (a)-(d), bulk electron densities for CrOx and Li_2O, the individual layers, and the overall size of the multilayer are provided for reference. To highlight the changing thickness of both oxide and metal layers, the individual metal, metal oxide, and lithiated phases are colored gray, blue, and red, respectively. In (e), the electron density is also defined by the color scale provided at the bottom of the plot.

thermodynamically unstable and is likely to decompose to more stable Cr and Cr_2O_3 phases.

The 3.3 V delithiation event is described by reaction iii, and both endmembers are shown in Figure 5c. We believe this reaction is similar to the intercalation reaction between $LiCrO_2$ and CrO_2 that has been reported at similar potentials with a comparable 5.5% volume change.[18] However, the species found in this reaction are likely amorphous, and the large 1.5 V hysteresis found between the redox peaks in Figure 4 could result from diffusion limitations and overpotentials associated with conversion. In this conditioned state, the multilayer expands even further during the second lithiation reaction, as seen in Figure 5d. Both the metal and oxide layers expand by ~75% from their initial thicknesses with the oxide layers reaching the theoretical density of Li_2O and the metal layers maintaining their original density. Compared to the first lithiation event (Figure 5b), the lithiated layers are more uniform in density suggesting that lithiation proceeds more uniformly, perhaps owing to lateral defects created by the significant volume changes during the first cycle. Such porosity may also explain the lower overall density in the metal layers than seen in the first cycle (Figure 5b). Nonetheless, the vertical modulation of the ML structure is even more ordered after the second lithiation reaction than at the start suggesting that the multilayer architecture may be beneficial for balancing

DOI: 10.1021/acs.chemmater.5b01809
Chem. Mater. 2016, 28, 47−54

Table 2. Changes in Average Oxide and Metal Layer Thicknesses at Each Condition Shown in Figure 5[a]

	average oxide layer thickness (Å)	average metal layer thickness (Å)
start	10.4(1)	11.1(1)
first lith (0.05 V)	15.6(7)	15.6(7)
first lith (1.0 V)	13.2(2)	14.9(2)
first delith (3.0 V)	11.0(1)	14.6(1)
first delith (3.5 V)	10.9(1)	13.5(1)
2nd lith (0.05 V)	18.2(3)	19.0(3)

[a]These numbers do not include the top metal layer which includes contributions from the adjacent $CrSi_2$ phase. Oxide and metal layers included in the table are labeled 1−10 in Figure 5a-b. The increase in thickness of the oxide layer during lithiation is due to the insertion of up to six Li per Cr_2O_3 molecule. The change in thickness of the metal layer confirms that the chemically neutral chromium plays a key role in reducing the CrO_x layer during lithiation.

strain, mass transport, and charge transfer in a conversion reaction.

Li Stoichiometry and Excess Charge. The electron density profiles also provide a complementary route for measuring the Li concentrations within the layered electrode structure. By comparing the integrated electron density in the multilayer region (Q_{XR}) to the initial condition, the number of additional charge species in the lithiated structure can be determined using

$$\Delta Q_{XR} = \frac{\int_0^{zML_f} \rho_{lithiated}(z)dz}{\int_0^{zML_i} \rho_{initial}(z)dz} \quad (1)$$

This quantity can be related to the conversion process itself using the additional charge from each lithium atom and the atomic number (Z) of each species in the reaction. This quantity can be directly converted to stoichiometry, assuming that the initial reactive species is Cr_2O_3. Using the atomic number (Z) of each species, we obtain the following relation for ΔQ_{XR}:

$$\Delta Q_{XR} = \frac{Z_{Cr_2O_3} + x_{Li}Z_{Li}}{Z_{Cr_2O_3}} \rightarrow x_{Li} = 24(\Delta Q_{XR} - 1) \quad (2)$$

For complete conversion, $x = 6$. Table 3 lists ΔQ_{XR} obtained using eq 2 for each condition shown in Figure 5. As expected from the volume changes given in Table 3, the additional electron density present after a complete cycle of lithaition and delithiation indicates that the process is somewhat irreversible at 3 V, nominally consistent with $LiCrO_2$, which would leave 1.5 Li per Cr_2O_3 molecular species. At 3.5 V, the structure contracts further, and the integrated electron density reaches the same value as the initial open circuit structure, indicating that (apparently) complete delithiation can be achieved with sufficiently large overpotentials.

Table 3. Change in Charge, Stoichiometry, and Volume in the CrO_x Regions Using XR Data[a]

	ΔQ_{XR}	x_{Li} (eq 2)	Δz (total)
first lithiation	1.407	9.77	46.3%
first delith (3 V)	1.080	1.92	15.6%
first delith (3.5 V)	0.991	−0.22	9.8%
second lithiation	1.285	6.84	54.9%

[a]The change in integrated charge density (ΔQ_{XR}) from the profiles in Figure 5b-d relative to the open circuit condition (Figure 5a) were used to calculate the additional Li stoichiometry using eq 2. For reference, the fractional volume change is also shown for each case. For reference, the theoretical volume change for $Cr_2O_3 \rightarrow 2Cr + 1.5Li_2O$ is 92%.

The amount of lithium inserted during each discharge (using eq 1 or 2) is actually larger than theoretically expected, consistent with the integrated charge measured during cyclic voltammetry (−0.0077 and −0.071 mAh for the first two cycles, well beyond the expected −0.057 mAhg for 20 nm of Si and 5 nm of Cr_2O_3). The observation of lithiation capacities that go beyond theoretical expectations is a well-known phenomenon in conversion materials and has beeen ascribed to a variety of mechanisms, including the following: (i) electrolyte decomposition;[19] (ii) a pseudocapacitive "polymeric/gel" species forming at low potentials;[20] (iii) the reduction of LiOH forming additional, active Li_2O species;[21] and (iv) a space-charge layer at the interface between the charged metal products and the Li-conducting Li_2O.[22] The results in Table 3 are derived from the *buried* electron density profiles of the CrO_x layers. Hence, mechansims (i), (ii), and (iii) which occur at the electrode surface likely do not play a significant role in these results (although they would contributed to the electrochemical signal). The remaining explanation involving a buildup of Li^+ in response to charge accumulation at the metal under anodic potentials could explain the additional charge (and expansion) measured by both the XR and electrochemical data, especially given the high concentration of buried interfaces in the model heterostructure. However, the 4 Å vertical resolution from the XR data is not sufficient to resolve these individual layers. The interfacial accumulation of lithia at the buried interfaces may explain the unexpectedly high density in the chromium-rich layers in Figure 4b, since XR is sensitive to the *change* in density across each interface. Higher resolution data (i.e., taken to higher momentum transfers) could provide a definitive answer to this mechanism.

Changes Related to Silicon and Sapphire. Beyond the pronounced structural changes found in the CrO_x conversion reaction, other components of the electrode also respond to lithiation. These changes can be seen in Figure 5(e), which shows the changes in ML electron density profiles from fits to the reflectivity during the first CV cycle. For example, the density of the silicon layer reduced by a factor of 2 at low potentials, in agreement with the reduced electron density of fully lithiated silicon ($Li_{22}Si_5$) (the thickness of the lithiated silicon layer was, however, difficult to identify due to its large surface roughness following lithiation and the similar electron densities of $Li_{22}Si$ and the electrolyte). The $CrSi_2$ layer at the Si/Cr interface, identified by TEM in Figure 2c, also undergoes a sudden reduction in density (starting at E = 0.17 V) associated with a conversion reaction, $CrSi_2 \rightarrow Cr + 2Li_xSi$. Upon lithiation, this region also shows a modulated structure, corresponding to phase-separated Li_xSi- and Cr-rich layers. Eventually the reduced chromium from this reaction coalesces with the top metal layer from the underlying ML structure (from 0.27 to 0.7 V). While insulating sapphire is not typically considered an active material for lithium batteries, electron density at the interface between the substrate and the bottom chromium layer was found to reversibly decrease in density at low potentials. This could involve lithium reacting with the

DOI: 10.1021/acs.chemmater.5b01809
Chem. Mater. 2016, 28, 47−54

oxygen-terminated surface of R-plane Al_2O_3[23] or possibly a ternary lithium aluminate phase as seen in studies involving amorphous alumina coatings on anodes using atomic layer deposition.[24,25]

CONCLUSIONS

We tracked the molecular-scale processes in a Li-conversion reaction of a model layered Cr/CrO_x thin film by combining electrochemistry with the interfacial sensitivity of *operando* X-ray reflectivity. In such a heterostructure, the electrochemically driven phase separation and recombination of the oxide into reduced Cr and lithiated Li_2O species is confined to one-dimension, preserving its layering throughout the subsequent electrochemical cycles. This structure enables a detailed view of the reactions and processes that are present at the interfaces between nanoscale species formed in bulk oxide electrodes. Such an intentionally layered structure provides a new strategy toward improving the structural and electrochemical reversibility of oxide conversion reactions by providing a pre-existing template (i.e., nucleation sites) for the reactions and controlling overpotentials. These *in situ* measurements provide new insights into the interplay between structural kinetics, volume changes, and chemical species of conversion reactions at the molecular scale.

ASSOCIATED CONTENT

Supporting Information

The Supporting Information is available free of charge on the ACS Publications website at DOI: 10.1021/acs.chemmater.5b01809.

Information related to the spectroelectrochemical cell, fitting procedures, and *ex situ* characterization (PDF)

AUTHOR INFORMATION

Corresponding Author

*E-mail: fister@anl.gov.

Present Address

[‖]School of Materials Engineering, Purdue University.

Author Contributions

The manuscript was written through contributions of all authors. All authors have given approval to the final version of the manuscript. Fister, Bedzyk, Gewirth, and Fenter conceived the experiment; Fister, Esbenshade, Chen, Long, Schlepütz, and Fenter performed XR and electrochemical measurements; Hu, Wu, Bedzyk, and Dravid performed TEM and XPS measurements; Shi grew the thin films.

Notes

The authors declare no competing financial interest.

ACKNOWLEDGMENTS

This work was supported as part of the Center for Electrochemical Energy Science, an Energy Frontier Research Center funded by the U.S. Department of Energy (DOE), Office of Science, Basic Energy Sciences (BES). Use of the Advanced Photon Source was supported by the U.S. Department of Energy, Office of Science, Office of Basic Energy Sciences, under Contract No. DE-AC02-06CH11357. The characterization work made use of the EPIC facility of the NUANCE Center-Northwestern University, which is partially supported by the NSF-MRSEC and NSF-NNCI programs; the International Institute for Nanotechnology (IIN); and the State of Illinois through IIN. Evguenia Karapetrova, Christopher Wolverton, Maria Chan, and John Vaughey provided valuable input.

ABBREVIATIONS

XR, X-ray reflectivity; ML, multilayer; CV, cyclic voltammetry; E, electrochemical potential relative to Li/Li^+; q, X-ray momentum transfer; q_c, critical momentum transfer for total reflection of X-rays; $R(q)$, intensity of the reflectivity

REFERENCES

(1) Whittingham, M. S. Lithium batteries and cathode materials. *Chem. Rev.* **2004**, *104*, 4271−4301.

(2) Poizot, P.; Laruelle, S.; Grugeon, S.; Dupont, L.; Tarascon, J. M. Nano-sized transition-metaloxides as negative-electrode materials for lithium-ion batteries. *Nature* **2000**, *407*, 496−499.

(3) Cabana, J.; Monconduit, L.; Larcher, D.; Palacin, M. R. Beyond Intercalation-Based Li-Ion Batteries: The State of the Art and Challenges of Electrode Materials Reacting Through Conversion Reactions. *Adv. Mater.* **2010**, *22*, E170−E192.

(4) Li, H.; Balaya, P.; Maier, J. Li-Storage via Heterogeneous Reaction in Selected Binary Metal Fluorides and Oxides. *J. Electrochem. Soc.* **2004**, *151*, A1878−A1885.

(5) Kasavajjula, U.; Wang, C.; Appleby, A. J. Nano- and bulk-silicon-based insertion anodes for lithium-ion secondary cells. *J. Power Sources* **2007**, *163*, 1003−1039.

(6) Zhang, W. J. Lithium insertion/extraction mechanism in alloy anodes for lithium-ion batteries. *J. Power Sources* **2011**, *196*, 877−885.

(7) Balaya, P.; Bhattacharyya, A. J.; Jamnik, J.; Zhukovskii, Y. F.; Kotomin, E. A.; Maier, J. Nano-ionics in the context of lithium batteries. *J. Power Sources* **2006**, *159*, 171−178.

(8) Larcher, D.; Masquelier, C.; Bonnin, D.; Chabre, Y.; Masson, V.; Leriche, J. B.; Tarascon, J. M. Effect of particle size on lithium intercalation into alpha-Fe2O3. *J. Electrochem. Soc.* **2003**, *150*, A133−A139.

(9) Wang, F.; Robert, R.; Chernova, N. A.; Pereira, N.; Omenya, F.; Badway, F.; Hua, X.; Ruotolo, M.; Zhang, R.; Wu, L.; Volkov, V.; Su, D.; Key, B.; Whittingham, M. S.; Grey, C. P.; Amatucci, G. G.; Zhu, Y.; Graetz, J. Conversion Reaction Mechanisms in Lithium Ion Batteries: Study of the Binary Metal Fluoride Electrodes. *J. Am. Chem. Soc.* **2011**, *133*, 18828−18836.

(10) Wiaderek, K. M.; Borkiewicz, O. J.; Pereira, N.; Ilavsky, J.; Amatucci, G. G.; Chupas, P. J.; Chapman, K. W. Mesoscale Effects in Electrochemical Conversion: Coupling of Chemistry to Atomic- and Nanoscale Structure in Iron-Based Electrodes. *J. Am. Chem. Soc.* **2014**, *136*, 6211−6214.

(11) Karapetrova, E.; Ice, G.; Tischler, J.; Hong, H. W.; Zschack, P. Design and performance of the 33-BM beamline at the Advanced Photon Source. *Nucl. Instrum. Methods Phys. Res., Sect. A* **2011**, *649*, 52−54.

(12) Tritsaris, G. A.; Zhao, K.; Okeke, O. U.; Kaxiras, E. Diffusion of Lithium in Bulk Amorphous Silicon: A Theoretical Study. *J. Phys. Chem. C* **2012**, *116*, 22212−22216.

(13) Balaya, P.; Li, H.; Kienle, L.; Maier, J. Fully reversible homogeneous and heterogeneous Li storage in RuO2 with high capacity. *Adv. Funct. Mater.* **2003**, *13*, 621−625.

(14) Dupont, L.; Grugeon, S.; Laruelle, S.; Tarascon, J. M. Structure, texture and reactivity versus lithium of chromium-based oxides films as revealed by TEM investigations. *J. Power Sources* **2007**, *164*, 839−848.

(15) Dupont, L.; Laruelle, S.; Grugeon, S.; Dickinson, C.; Zhou, W.; Tarascon, J. M. Mesoporous Cr2O3 as negative electrode in lithium batteries: TEM study of the texture effect on the polymeric layer formation. *J. Power Sources* **2008**, *175*, 502−509.

(16) Luo, L.; Wu, J.; Xu, J.; Dravid, V. P. Atomic Resolution Study of Reversible Conversion Reaction in Metal Oxide Electrodes for Lithium-Ion Battery. *ACS Nano* **2014**, *8*, 11560−11566.

(17) Su, Q.; Xie, D.; Zhang, J.; Du, G.; Xu, B. In Situ Transmission Electron Microscopy Observation of the Conversion Mechanism of

DOI: 10.1021/acs.chemmater.5b01809
Chem. Mater. 2016, 28, 47−54

Fe2O3/Graphene Anode during Lithiation−Delithiation Processes. *ACS Nano* **2013**, *7*, 9115−9121.
(18) Komaba, S.; Takei, C.; Nakayama, T.; Ogata, A.; Yabuuchi, N. Electrochemical intercalation activity of layered NaCrO2 vs. LiCrO2. *Electrochem. Commun.* **2010**, *12*, 355−358.
(19) Ponrouch, A.; Taberna, P. L.; Simon, P.; Palacin, M. R. On the origin of the extra capacity at low potential in materials for Li batteries reacting through conversion reaction. *Electrochim. Acta* **2012**, *61*, 13−18.
(20) Laruelle, S.; Grugeon, S.; Poizot, P.; Dollé, M.; Dupont, L.; Tarascon, J.-M. On the Origin of the Extra Electrochemical Capacity Displayed by MO/Li Cells at Low Potential. *J. Electrochem. Soc.* **2002**, *149*, A627−A634.
(21) Hu, Y.-Y.; Liu, Z.; Nam, K.-W.; Borkiewicz, O. J.; Cheng, J.; Hua, X.; Dunstan, M. T.; Yu, X.; Wiaderek, K. M.; Du, L.-S.; Chapman, K. W.; Chupas, P. J.; Yang, X.-Q.; Grey, C. P. Origin of additional capacities in metal oxide lithium-ion battery electrodes. *Nat. Mater.* **2013**, *12*, 1130−1136.
(22) Jamnik, J.; Maier, J. Nanocrystallinity effects in lithium battery materials - Aspects of nano-ionics. Part IV. *Phys. Chem. Chem. Phys.* **2003**, *5*, 5215−5220.
(23) Catalano, J. G.; Park, C.; Zhang, Z.; Fenter, P. Termination and water adsorption at the alpha-Al2O3 (012) - Aqueous solution interface. *Langmuir* **2006**, *22*, 4668−4673.
(24) Xiao, X.; Lu, P.; Ahn, D. Ultrathin Multifunctional Oxide Coatings for Lithium Ion Batteries. *Adv. Mater.* **2011**, *23*, 3911−3915.
(25) Leung, K.; Qi, Y.; Zavadil, K. R.; Jung, Y. S.; Dillon, A. C.; Cavanagh, A. S.; Lee, S.-H.; George, S. M. Using Atomic Layer Deposition to Hinder Solvent Decomposition in Lithium Ion Batteries: First-Principles Modeling and Experimental Studies. *J. Am. Chem. Soc.* **2011**, *133*, 14741−14754.

DOI: 10.1021/acs.chemmater.5b01809
Chem. Mater. 2016, 28, 47−54